

# Microstructural evolution and mechanical properties of in *situ nano* Ta<sub>4</sub>HfC<sub>5</sub> reinforced SiBCN composite ceramics

**Bingzhu Wang**

Harbin Institute of Technology

**Li Daxin** (✉ [lidaxin@hit.edu.cn](mailto:lidaxin@hit.edu.cn))

Harbin Institute of Technology <https://orcid.org/0000-0003-4930-0031>

**Zhijia Yang**

Harbin Institute of Technology

**Dechang Jia**

Harbin Institute of Technology

**Jingyi Guan**

Harbin Institute of Technology

**Hao Peng**

Harbin Institute of Technology

**Delong Cai**

Harbin Institute of Technology

**Peigang He**

Harbin Institute of Technology

**Xiaoming Duan**

Harbin Institute of Technology

**Yu Zhou**

Harbin Institute of Technology

---

## Research Article

**Keywords:** Ta<sub>4</sub>HfC<sub>5</sub>; SiBCN; Microstructure evolution; Mechanical properties

**Posted Date:** June 29th, 2020

**DOI:** <https://doi.org/10.21203/rs.3.rs-17623/v2>

**License:** © ⓘ This work is licensed under a Creative Commons Attribution 4.0 International License.

[Read Full License](#)

**Version of Record:** A version of this preprint was published at Journal of Advanced Ceramics on November 27th, 2020. See the published version at <https://doi.org/10.1007/s40145-020-0410-9>.

# Abstract

In this paper, the *in situ* nano Ta<sub>4</sub>HfC<sub>5</sub> reinforced SiBCN-Ta<sub>4</sub>HfC<sub>5</sub> composite ceramics were prepared by a combination of two-step mechanical alloying and reactive hot-pressing sintering. The microstructural evolution and mechanical properties of the resulting SiBCN-Ta<sub>4</sub>HfC<sub>5</sub> were studied. After the first-step milling of 30 h, the raw materials of TaC and HfC undergone crushing, cold sintering and short-range interdiffusion to finally obtain the high pure nano Ta<sub>4</sub>HfC<sub>5</sub>. A hybrid structure of amorphous SiBCN and nano Ta<sub>4</sub>HfC<sub>5</sub> was obtained by adopting a second-step ball-milling. After reactive hot-pressing sintering, amorphous SiBCN has crystallized to nano SiC and turbostratic BN(C) phases while Ta<sub>4</sub>HfC<sub>5</sub> retained the form of nano structure. With the *in situ* generation of 2.5 wt% Ta<sub>4</sub>HfC<sub>5</sub>, Ta<sub>4</sub>HfC<sub>5</sub> is preferentially distributed within the turbostratic BN(C); however, as Ta<sub>4</sub>HfC<sub>5</sub> content further raised to 10 wt%, it mainly distributed in the grain-boundary of BN(C) and SiC. *The introduction of Ta<sub>4</sub>HfC<sub>5</sub> nanocrystals can effectively improve the flexural strength and fracture toughness of SiBCN ceramics, reaching to 344.1 MPa and 4.52 MPa·m<sup>1/2</sup>, respectively.* This work has solved the problems of uneven distribution of ultra-high temperature phase in ceramic matrix, which is beneficial to the real applications of SiBCN ceramics.

## Introduction

With the development of aerospace technology, more stringent properties requirements are put forward for advanced structural-functional integration ceramic materials. Among many high-temperature structural materials, SiBCN non-oxide ceramics have attracted considerable attention due to their light-weight, high specific strength, excellent thermal stability and resistance to thermal shock, oxidation and ablation [1-3].

Polymer/precursor derived ceramics (PDCs), one of the very first route to prepare SiBCN materials, remain amorphous nature at least up to 1400 °C, and do not undergo microstructural changes at this temperature [3]. The chemistry, microstructure and properties of the PDCs SiBCN can be tailored effectively by controlling the initial reagent structure, chemical reaction and processing parameters [4]. Unfortunately, this method also has some nonnegligible shortcomings that limit its wide applications. The starting materials (such as SiCl<sub>3</sub>CH<sub>3</sub>, BCl<sub>3</sub>, etc.) are usually expensive and some organic solvents used are harmful to human health and the environment [5]. During pyrolysis, the gases release and mass loss requires careful monitoring to avoid porous structure and to carefully control shrinkage (even microcracks) [5-7].

Mechanical alloying and solid-state sintering techniques (also referred as inorganic method) to obtain dense nano or amorphous SiBCN monoliths and their ceramic composites were proposed [6]. One of the significant advantages of this processing route is to provide centimeter-sized samples convenient for evaluating the basic mechanical and thermophysical properties [7-8]. However, the previous studies showed that the heterogeneous microstructure leading to poor mechanical properties of the SiBCN ceramics are needed to be further optimized for the real applications at high-temperatures [9,10].

As documented, the introduction of ultra-high temperature ceramics (UHTCs) into SiBCN ceramic matrix, is believed to be an effective strategy to improve the mechanical performance of SiBCN ceramics [11-14]. In previous attempts, the microstructural evolution and thermal stability of the porous PDCs ZrB<sub>2</sub>-SiBCN and HfN-SiBCN composite ceramics have been investigated [21,22]. However, due to the limitation of sample size, the mechanical properties of these composite ceramics have not been evaluated. In another contribution, Liang et al. [15-17] has introduced some LaB<sub>6</sub> into SiBCN matrix by the inorganic method, obtaining desirable mechanical properties as compared with pure SiBCN. However, during the sintering process, some LaB<sub>6</sub> has reacted with SiBCN ceramic matrix to generate La<sub>2</sub>B<sub>2</sub>C<sub>6</sub> and consequently, the strengthening and toughening effects of LaB<sub>2</sub> were significantly reduced. Further, Miao et al. [18-20] has prepared SiBCN-ZrB<sub>2</sub> composite ceramics by mechanical alloying combined with sol-gel method. The results suggested that the *in-situ* ZrB<sub>2</sub> can improve the mechanical properties of SiBCN ceramic materials to some extent; however, the particle size of the *in-situ* ZrB<sub>2</sub> has grown up to a maximum value of ~1 μm.

Generally, the following factors should be considered when the external UHTCs are selected as reinforcements in SiBCN ceramics: (i) they should not react with SiBCN matrix to form strong bonding interfacial structure during annealing or sintering; (ii) they could be uniformly dispersed in ceramic matrix in the form of nanocrystals and (iii) are supposed to have good physical-chemical compatibility with SiBCN.

The chemically stable Ta<sub>4</sub>HfC<sub>5</sub>, the current highest melting point compound, was theoretical forecasted by Agte et al. [23] and experiment confirmed by Andrievskii et al. [24]. Up to present, various strategies are used to the synthesis of the high pure Ta<sub>4</sub>HfC<sub>5</sub>. For example, Simonenko et al. [25] has reported a sol-gel technology for preparing Ta<sub>4</sub>HfC<sub>5</sub> by using metal oxide and gel of polymeric carbon source. The polymeric carbon source undergo preliminary annealing to provide a uniform dispersion of metal oxide-carbon mixture, and then further heating to 1200~1500 °C to obtain pure Ta<sub>4</sub>HfC<sub>5</sub>. Liu et al. [26] used the Hf and Ta containing polyantahafnoxane modified with allyl-functional novolac resin to produce Ta<sub>4</sub>HfC<sub>5</sub> polymer (polyantahafnoxanesal). The resulting polyantahafnoxanesal is subsequently solidified and pyrolyzed at 1400 °C to obtain pure Ta<sub>4</sub>HfC<sub>5</sub>. These methods, of course, are very effective to prepare pure Ta<sub>4</sub>HfC<sub>5</sub> with high thermal stability and chemical stability; however, these processing methods often contain complex synthesis steps leading to high-cost products. The raw materials used are also flammable and present waste disposal problems. For this reason, Osama et al. [27] have successfully prepared nano Ta<sub>4</sub>HfC<sub>5</sub> by mechanical alloying for the first time. However, the formation mechanisms of the mechanical alloying derived nano Ta<sub>4</sub>HfC<sub>5</sub> is still unclear. And the research on Ta<sub>4</sub>HfC<sub>5</sub>/SiBCN composite ceramics has not been report yet.

Thus, in this work, initially, the Ta<sub>4</sub>HfC<sub>5</sub> nanocrystals were prepared by mechanical alloying method and then SiBCN-Ta<sub>4</sub>HfC<sub>5</sub> amorphous-nanocrystalline composite ceramic powder was prepared by a second step of mechanical alloying. Afterward, the hot-pressing sintering technology was adopted to consolidate

SiBCN-Ta<sub>4</sub>HfC<sub>5</sub> composite ceramics. As expected, the homogeneous distribution of nano Ta<sub>4</sub>HfC<sub>5</sub> within the SiBCN ceramic matrix strongly improved the mechanical properties of the composite ceramics. The formation mechanisms of mechanical alloying derived nano Ta<sub>4</sub>HfC<sub>5</sub>, and the correlation of microstructural evolution and mechanical properties of the resulting SiBCN-Ta<sub>4</sub>HfC<sub>5</sub> composite ceramics were illustrated.

## Materials And Methods

### 2.1 Raw materials

Hexagonal boron nitride (h-BN, 99.0% purity, 0.6 μm, purchased from Advanced Technology & Materials Co., Ltd), graphite (99.5% purity, 8.7 μm, purchased from Qingdao Huatai Lubricant Sealing S&T Co., Ltd), cubic silicon (c-Si, 99.9% purity, 9.0 μm, purchased from China New Metal Materials Technology Co., Ltd.), hafnium carbide (HfC, 99.0% purity, 1 μm, purchased from Shanghai Puwei Applied Materials Technology Co., Ltd) and tantalum carbide (TaC, 99.0% purity, 1 μm, purchased from Shanghai Puwei Applied Materials Technology Co., Ltd) were used here as received.

### 2.2 Synthesis of Ta<sub>4</sub>HfC<sub>5</sub> nanocrystals

*Ta<sub>4</sub>HfC<sub>5</sub> nanocrystals were prepared by mechanical alloying method via a P4 high-energy ball-miller manufactured by FRITSCHE company. Firstly, TaC and HfC mixed powders with a molar ratio of 4:1 were poured into the ball milling tanks filled with argon, and then subjected to different hours of milling. The ball-to-powder mass ratio was set as 20: 1 and the effective ball-milling time was X h (X=0.5, 1, 1.5, 2, 3, 5, 10, 20, 30 h). The main disc was rotated at 350 rpm while the vials were rotated at 800 rpm in reverse.*

### 2.3 Synthesis of SiBCN-Ta<sub>4</sub>HfC<sub>5</sub> powder and bulk ceramics

*In this stage, c-Si, h-BN, graphite and Ta<sub>4</sub>HfC<sub>5</sub> nanocrystals were put into ball milling tanks. Among them the molar ratio of Si: BN: C is 2: 1: 3, and Ta<sub>4</sub>HfC<sub>5</sub> nanocrystals accounts for 0 wt%, 2.5 wt%, 5 wt%, 10 wt% and 15 wt% of the total mass of powder in the ball milling tank respectively. During the milling process, the rotation speed of the main disc was set at 350 rpm while the vials were rotated at 600 rpm in reverse. In this scene, the effective milling time of 20 h could ensure a well-defined microstructure of the mixtures<sup>[28-29]</sup>. The powders mixed, stored and transported were conducted in high pure Ar.*

*SiBCN-Ta<sub>4</sub>HfC<sub>5</sub> mixed powders were loaded into a graphite mould with a diameter of 36 mm, and then sintered via the hot-pressing sintering system (50-250T model, AVS company, USA). The sintering was conducted at a temperature of 1900 °C and holding time for 1 h under an axial pressure of 60 MPa. The content of Ta<sub>4</sub>HfC<sub>5</sub> in SiBCN-Ta<sub>4</sub>HfC<sub>5</sub> composite ceramics is 0 wt%, 2.5 wt%, 5 wt%, 10 wt% and 15 wt%, respectively.*

### 2.4 Characterization

The phase composition of the samples was measured by X'PERT X-ray diffractometer purchased from Panalytical Company of Netherlands. The scanning speed is  $10^\circ/\text{min}$  and the scanning range is  $10^\circ\text{-}90^\circ$ . The morphologies of the samples were observed by using NanoLab 600i scanning electron microscope produced by FEI company. Tecnai G2 F20 transmission electron microscope from FEI company was used to observe the microstructure of  $\text{Ta}_4\text{HfC}_5$  and  $\text{SiBCN-Ta}_4\text{HfC}_5$  powders. The microstructure and element distribution of the  $\text{SiBCN-Ta}_4\text{HfC}_5$  composite ceramics were investigated by using Talos f200x transmission electron microscope produced by FEI company. The Raman spectra were collected via an inVia-Reflex testing system manufactured by RENISHAW company, with the excitation wavelength of 785 nm.

## Results And Discussion

### 3.1 Synthesis and characterization of nano $\text{Ta}_4\text{HfC}_5$ powder

Prior to mechanical alloying, the powder mixture of the TaC-HfC show sharp diffraction peaks (Fig. 1). After 0.5 h of milling, the intensities of the corresponding diffraction peaks are reduced and the full width at half maximum (FWHM) becomes wider. This should be argued to the grain refinement of TaC and HfC<sup>[30]</sup>. As the milling time further raises to 1~5 h, TaC and HfC gradually undergo solid solution reaction to form  $\text{Ta}_4\text{HfC}_5$ . Interestingly, the single-phase  $\text{Ta}_4\text{HfC}_5$  solid solution is obtained after mechanical alloying for 10 h. Further prolonging the milling time to 20~30 h, the diffraction peaks of the as-prepared  $\text{Ta}_4\text{HfC}_5$  gradually decrease, implying the grain refinement of  $\text{Ta}_4\text{HfC}_5$ .

After mechanical alloying, the diffraction peaks of the as-prepared  $\text{Ta}_4\text{HfC}_5$  shifting to the small angle direction result from the radius difference between Hf and Ta, which can be depicted by the Vegard's law: (see Equation 1 in the Supplementary Files)

Where  $a$ ,  $a_1$  and  $a_2$  represent the lattice constant of the new forming solid solution, and the two starting components, respectively. The  $c_1$  and  $c_2$  represent the concentration of the two starting components, respectively<sup>[31-33]</sup>. The radius of the Hf is bigger than that of Ta. Thus, the short-range diffusion of Hf atoms into the interstitial sites of Ta can lead to the expansion of TaC lattice (Fig. 2).

TEM analysis confirm the raw materials of TaC and HfC powders both have relatively large grain size [Fig. 3(a) and (b)]. Besides, the corresponding SAED pattern displays some diffraction spots and rings of HfC and TaC [Fig. 3(c)]. After ball milling for only 0.5 h, the grain size of TaC and HfC decreases obviously and some diffraction spots of TaC and HfC have disappeared [Fig. 3(d-f)]. Notably, at this milling time, mechanical alloying has induced many structural defects in both TaC and HfC, which can provide conveniently channel for Hf atoms diffused inward. With a progressing milling of 30 h, only pure  $\text{Ta}_4\text{HfC}_5$  nanocrystals are obtained without any trace of HfC or below the limits of detection [Fig. 3(g-i)]. For pure TaC ball-milled for 30 h [Fig. 3(j-l)], SAED pattern with bright-spots and narrow-rings verifies the well-defined crystalline phase of TaC.

The SEM surface morphologies in Fig. 4(a) further ensure that the raw materials of TaC-HfC powder mixture have larger particle size. Nevertheless, after mechanical alloying for 0.5 h, the particle size of the powder mixture decreases obviously, which is mainly composed of nano-particles [Fig. 4(b)]. With the progress of mechanical alloying (1.5-30 h), these particles are continuously deformed, crushed and cold sintered; however, the morphologies of the resulting particles are almost unchanged. The EDS maps in Fig. 4(f)-(i) confirm that the Ta, Hf and C atoms distribute uniformly after 30 h of milling, suggesting a good solid solubility of Hf into TaC.

Fig. 5 shows the XRD patterns of the *in situ* SiBCN-Ta<sub>4</sub>HfC<sub>5</sub> amorphous-nanocrystalline composite powder with different Ta<sub>4</sub>HfC<sub>5</sub> content. After 20 h of mechanical alloying, the lattice structure of c-Si, h-BN and graphite was destroyed to form amorphous SiBCN. Besides, the broad diffraction peaks of Ta<sub>4</sub>HfC<sub>5</sub> were observed, and these peak intensities gradually increase with the increase of Ta<sub>4</sub>HfC<sub>5</sub> content. Confidentially, the nano Ta<sub>4</sub>HfC<sub>5</sub> does not react with other component of SiBCN and still presents the form of nanocrystals ~ 3-5 nm in the amorphous matrix after mechanical alloying (Fig. 6).

The formation mechanisms of the mechanical alloying derived nano Ta<sub>4</sub>HfC<sub>5</sub> are elaborated in Fig. 7. During the mechanical alloying process, the sample particles are continuously deformed, crushed and cold sintered under mechanical impact conditions, which led to grain refinement and microstrain occurring in the crystal grains. The dislocation density can be represented by the following equation [34]: (see Equation 3 in the Supplementary Files)

Where  $\epsilon$  is the microstrain,  $D$  is the grain size, and  $b$  is the Burgers vector. According to formula (2), larger microstrain and smaller grain size lead to higher dislocation density in the crystal. Besides, the decrease in grain size results in an increase in surface area per unit volume. Higher surface energy provides driving force for diffusion, while more defects provide channels for atom diffusion. Therefore, a uniform solid solution of Ta<sub>4</sub>HfC<sub>5</sub> was formed.

### 3.2 Microstructural evolution and mechanical properties of as-sintered SiBCN-Ta<sub>4</sub>HfC<sub>5</sub> composite ceramics

After reactive hot-pressing sintering, SiBCN-Ta<sub>4</sub>HfC<sub>5</sub> composite ceramics mainly consists of BN(C),  $\beta$ -SiC,  $\alpha$ -SiC and Ta<sub>4</sub>HfC<sub>5</sub> (Fig. 8). Obviously, the intensity of the diffraction peaks of the Ta<sub>4</sub>HfC<sub>5</sub> is positively correlated with the content of Ta<sub>4</sub>HfC<sub>5</sub>. Interestingly, with the increase of Ta<sub>4</sub>HfC<sub>5</sub> content, the diffraction peaks of  $\alpha$ -SiC decrease while the diffraction peaks of  $\beta$ -SiC increase. This thus means that the *in situ* Ta<sub>4</sub>HfC<sub>5</sub> affects the  $\beta \rightarrow \alpha$  transition of SiC.

Fig. 9 exhibits the Raman spectra of the as-sintered SiBCN-Ta<sub>4</sub>HfC<sub>5</sub> composite ceramics with various Ta<sub>4</sub>HfC<sub>5</sub> content. Two Raman peaks in a range of 60-260 cm<sup>-1</sup> are gradually enhanced with the increase content of the *in situ* Ta<sub>4</sub>HfC<sub>5</sub>. The emergence of Raman peak at 1374 cm<sup>-1</sup> results from the D-side peak

edge of graphite and the scattering peak of h-BN [5]. However, the generation of Raman peak at  $1588\text{ cm}^{-1}$  should be assigned to the G-side peak of graphite [35].

After hot-pressing sintering, amorphous SiBCN has crystallized to product turbostratic BN(C) and nano SiC (Fig. 10). For pure SiBCN, BN(C) phase is distributed at the grain boundaries of SiC grains. Besides, the Si elements are mainly distributed in SiC grains, while B, C and N elements are distributed in the form of BN(C) phase at SiC grain boundaries. With 2.5 wt% Ta<sub>4</sub>HfC<sub>5</sub> addition, most of the Ta<sub>4</sub>HfC<sub>5</sub> ~10 nm are distributed in BN(C) phase in the form of nanocrystals (Fig. 11). The Ta<sub>4</sub>HfC<sub>5</sub> grains are thereby separated by BN(C). This structure is beneficial to the grain refinement of Ta<sub>4</sub>HfC<sub>5</sub> and constrains short-range diffusion of the atoms. The EDS maps of the selective region in Ta<sub>4</sub>HfC<sub>5</sub>-BN(C) clearly show that the Ta, Hf and some C elements are distributed in Ta<sub>4</sub>HfC<sub>5</sub> phase, while the rest of C elements are distributed in BN(C) phase (Fig. 12). With 10 wt% Ta<sub>4</sub>HfC<sub>5</sub> addition, a part of nano Ta<sub>4</sub>HfC<sub>5</sub> ~10 nm is still uniformly distributed in BN(C), while other nano Ta<sub>4</sub>HfC<sub>5</sub> >10 nm is randomly distributed in ceramic matrix (Fig. 13). The microstructural evolution diagram of the SiBCN-Ta<sub>4</sub>HfC<sub>5</sub> composite ceramics with different Ta<sub>4</sub>HfC<sub>5</sub> content is displayed in Fig. 14.

The flexural strength and fracture toughness of the as-sintered SiBCN-Ta<sub>4</sub>HfC<sub>5</sub> composite ceramics are shown in Fig. 15. Apparently, the introduction of Ta<sub>4</sub>HfC<sub>5</sub> nanocrystals has effectively improved the flexural strength and fracture toughness of the SiBCN ceramics. For pure SiBCN ceramics, they only show flexural strength of 156.1 MPa and fracture toughness of  $1.82\text{ MPa}\cdot\text{m}^{1/2}$ , respectively. With 10 wt% Ta<sub>4</sub>HfC<sub>5</sub> addition, the composite ceramics possess optimized flexural strength reaching to 344.1 MPa, while the composite ceramics with 5 wt% Ta<sub>4</sub>HfC<sub>5</sub> obtain fracture toughness of  $4.52\text{ MPa}\cdot\text{m}^{1/2}$ .

## Conclusion

In this study, SiBCN-Ta<sub>4</sub>HfC<sub>5</sub> composite ceramics were prepared by two-step mechanical alloying combined with reactive hot-pressing sintering. After the above analysis, the following conclusions can be drawn:

(1) In the initial step of mechanical alloying of 30 h, TaC-HfC powder mixture are crushed, cold sintered and interdiffused, and finally forming Ta<sub>4</sub>HfC<sub>5</sub> nanocrystalline. After the second step of milling for 20 h, a hybrid structure of amorphous SiBCN and nano Ta<sub>4</sub>HfC<sub>5</sub> can be obtained. The lattice structures of C-Si, h-BN and graphite were destroyed to form amorphous structures. However, Ta<sub>4</sub>HfC<sub>5</sub> is uniformly distributed in amorphous powder in the form of nanocrystals.

(2) After reactive hot-pressing sintering, SiBCN-Ta<sub>4</sub>HfC<sub>5</sub> composite ceramics mainly contain Ta<sub>4</sub>HfC<sub>5</sub>, BN(C), β-SiC and α-SiC. The Ta<sub>4</sub>HfC<sub>5</sub> still exists in the form of nanocrystalline and does not react with the SiBCN matrix composition. With only 2.5 wt% Ta<sub>4</sub>HfC<sub>5</sub> addition, nano Ta<sub>4</sub>HfC<sub>5</sub> is preferentially distributed

in BN(C) phase; however, it tends to both distribute in BN(C) phase and ceramic matrix when 10 wt% Ta<sub>4</sub>HfC<sub>5</sub> is adopted.

(3) The introduction of the Ta<sub>4</sub>HfC<sub>5</sub> nanocrystals can effectively improve the flexural strength and fracture toughness of SiBCN ceramics due to the grain refinement and uniform distribution of nano Ta<sub>4</sub>HfC<sub>5</sub>. SiBCN ceramics with 10 wt% Ta<sub>4</sub>HfC<sub>5</sub> present optimized flexural strength of 344.1 MPa, while composite ceramics with 5 wt% Ta<sub>4</sub>HfC<sub>5</sub> obtain fracture toughness of 4.52 MPa·m<sup>1/2</sup>.

## Declarations

### Acknowledgements

Financial support from the National Natural Science Foundation of China under grant numbers of 51621091, 51472059, 51225203 and 51272300 is much appreciated. This work is also funded by National Key Research and Development Program (Grant No. 2017YFB0310400), Postdoctoral Innovative Talents Support Program with Grant No BX20190095 and China Postdoctoral Science Foundation under grant numbers of 2019M660072.

## References

- [1] R. Riedle, A. Kienzle, W. Dressler, L. Ruwisch, J. Bill, F. Aldinger, A Silicoboron Carbonitride Ceramic Stable to 2000 °C, *Nature* 382 (1996) 796-798.
- [2] R. Riedle, L.M. Ruswisch, L. An, R. Raj, Amorphous silicoboron carbonitride ceramic with very high viscosity at temperatures above 1500°C, *Journal of the American Ceramic Society* 81 (2005) 3341-3344.
- [3] N.V.R. Kumar, S. Prinz, C. Ye, A. Zimmermann, F. Aldinger, F. Berger, K. Müller, Crystallization and creep behavior of Si–B–C–N ceramics, *Acta Materialia* 53 (2005) 4567-4578.
- [4] T.G. Babu, R. Devasia, Simple and low-cost synthetic route for SiBCN ceramic powder from a boron modified cyclotrisilazane, *Journal of the American Ceramic Society* 102 (2019) 476-489.
- [5] C. Song, X. Liu, F. Ye, Y. Liu, L. Cheng, Mechanical and dielectric properties of SiC<sub>f</sub>/BN/SiBCN composites via different synthesis technologies, *Journal of the European Ceramic Society* 39 (2019) 4417-4423.
- [6] D. Jia, B. Liang, Z. Yang, Z. Yu, Metastable Si-B-C-N ceramics and their matrix composites developed by inorganic route based on mechanical alloying: Fabrication, microstructures, properties and their relevant basic scientific issues, *Progress in Materials Science* 98 (2018) 1-67.
- [7] D. Li, Q. Li, J. Yuan, Z. Yang, D. Jia, D. Cai, S. Wang, Y. Zhou, D. Yu, Y. Tian, Effects of high pressure on the low-temperature sintering of dense amorphous SiBCN monoliths, *Journal of the European Ceramic Society* 38 (2018) 3777-3786.

- [8] P. Zhang, D. Jia, Z. Yang, X. Duan, Y. Zhou, Progress of a novel non-oxide Si-B-C-N ceramic and its matrix composites, *Journal of Advanced Ceramics* 1 (2012) 157-178.
- [9] J. Wang, X. Duan, Z. Yang, D. Jia, Y. Zhou, Ablation mechanism and properties of SiC<sub>f</sub>/SiBCN ceramic composites under an oxyacetylene torch environment, *Corrosion Science* 82 (2014) 101-107.
- [10] D. Li, Z. Yang, D. Jia, X. Duan, P. He, Y. Zhou, Ablation behavior of graphene reinforced SiBCN ceramics in an oxyacetylene combustion flame, *Corrosion Science* 100 (2015) 85-100.
- [11] N. Liao, D. Jia, Z.H. Yang, B. Niu, Y. Zhou, Y. Li, Enhanced mechanical properties, thermal shock resistance and ablation resistance of Si<sub>2</sub>BC<sub>3</sub>N ceramics with nano ZrB<sub>2</sub> addition, *Journal of the European Ceramic Society* 39 (2019) 846-859.
- [12] B. Feng, Y. Zhang, B. Li, Medium-temperature sintering efficiency of ZrB<sub>2</sub> ceramics using polymer-derived SiBCN as a sintering aid, *Journal of the European Ceramic Society* 102 (2019) 855-866.
- [13] S. Wang, Y. Zhang, Y. Sun, Synthesis and characteristic of SiBCN/HfN ceramics with high temperature oxidation resistance, *Journal of Alloys and Compounds* 685 (2016) 828-835.
- [14] M. Sun, R. Fu, J. Chen, Fabrication and microstructures of functional gradient SiBCN-Nb composite by hot pressing, *Materials Characterization* 114 (2019) 115-121.
- [15] B. Liang, Z. Yang, D. Jia, S. Guo, Q. Zhu, X. Liao, Y. Miao, Q. Zhang, Y. Zhou, Densification, microstructural evolution and mechanical properties of Si-B-C-N monoliths with LaB<sub>6</sub> addition, *Journal of Alloys and Compounds* 696 (2017) 1090-1095.
- [16] B. Liang, Z. Yang, Y. Miao, Q. Zhu, X. Liao, Q. Li, Z. Tian, D. Jia, Y. Zhou, Si-B-C-N monoliths with LaB<sub>6</sub>-induced well-developed BN(C) flakes, *Materials Letters* 187 (2017) 36-39.
- [17] B. Liang, Z. Yang, Y. Miao, Q. Li, Q. Zhu, X. Liao, D. Jia, Y. Zhou, Microstructural evolution, mechanical and thermal properties of LaB<sub>6</sub> embedded in Si-B-C-N prepared by spark plasma sintering, *Ceramics International*. 43 (2017) 4814-4820.
- [18] Y. Miao, Z. Yang, B. Liang, Q. Li, Q. Chen, D. Jia, Y.B. Cheng, Y. Zhou, A novel in situ synthesis of SiBCN-Zr composites prepared by a sol-gel process and spark plasma sintering, *Dalton Transactions*. 45 (2016) 12739-12744.
- [19] Y. Miao, Z. Yang, J. Rao, X. Duan, P. He, D. Jia, Y. Cheng, Y. Zhou, Influence of sol-gel derived ZrB<sub>2</sub> additions on microstructure and mechanical properties of SiBCN composites, *Ceramics International*. 43 (2017) 4372-4378.
- [20] Y. Miao, Z. Yang, Q. Zhu, B. Liang, L. Quan, T. Zhuo, D. Jia, Y.B. Cheng, Z. Yu, Thermal ablation behavior of SiBCN-Zr composites prepared by reactive spark plasma sintering, *Ceramics International*. 43

(2017) 7978-7983.

- [21] B. Feng, Y. Zhang, B. Li, S. Hu, Medium-temperature sintering efficiency of  $ZrB_2$  ceramics using polymer-derived SiBCN as a sintering aid, *Journal of the American Ceramic Society*. 102 (2019) 855–866.
- [22] S. Wang, Y. Zhang, S. Yong, X. Yao, Y. Ming, Synthesis and characteristic of SiBCN/HfN ceramics with high temperature oxidation resistance, *Journal of Alloys and Compounds*. 685 (2016) 828–835.
- [23] Agte C, Alterthum H, Investigations of the High-Melting Carbide Systems Connected with Problem of the Carbon Melting, *Z. Techn. Phys.* 11 (1930) 182.
- [24] Andrievskii R A, Strel'Nikova N S, Poltoratskii N I, Melting point in systems ZrC-HfC, TaC-ZrC, TaC-HfC, *Soviet Powder Metallurgy & Metal Ceramics*. 6 (1967) 65-67.
- [25] E. P. Simonenko, N. A. Ignatov, N. P. Simonenko, Yu. S. Ezhov, V. G. Sevastyanov, N. T. Kuznetsov, Zirconium Carbide  $Ta_4ZrC_5$  and Tantalum–Hafnium Carbide  $Ta_4HfC_5$  via Sol–Gel Technology, *Synthesis and Properties of Inorganic Compounds*. 56 (2011) 1763-1769.
- [26] Y. Lu, Y. Sun, T. Zhang, F. Chen, L. Ye, T. Zhao, Polymer-derived  $Ta_4HfC_5$  nanoscale ultrahigh-temperature ceramics: Synthesis, microstructure and properties, *Journal of the European Ceramic Society*. 39 (2019) 205-211.
- [27] Osama Gaballa, B.A. Cook, A.M. Russell, Reduced-temperature processing and consolidation of ultra-refractory  $Ta_4HfC_5$ , *Int. Journal of Refractory Metals and Hard Materials*. 41 (2013) 293-299
- [28] N. Liao, D. Jia, Z. Yang, Y. Zhou, Y. Li, X. Jia, Strengthening and toughening effects of MWCNTs on  $Si_2BC_3N$  ceramics sintered by SPS technique, *Materials Science and Engineering A*. 710 (2018) 142-150.
- [29] N. Liao, D. Jia, Z. Yang, Z. Yu, Y. Li, Mechanical properties and thermal shock resistance of  $Si_2BC_3N$  ceramics with ternary  $Al_4SiC_4$  additive, *Ceramics International*. 44 (2018) 9009-9017.
- [30] K. Pierre M, D Simon, M Maaza, C. Liu, R. Mohamed M, R. Diaa A, M. Bonex W, Strain and grain size of  $TiO_2$  nanoparticles from TEM, Raman spectroscopy and XRD: The revisiting of the Williamson-Hall plot method, *Results in Physics*. 9 (2018) 628-635.
- [31] H. Chen, B. Tang, C. Zhong, Y. Yuan, Y. Tan, S. Zhang, The dielectric constant and quality factor calculation of the microwave dielectric ceramic solid solutions, *Ceramics International*. 43(2017) 7383-7386.
- [32] Q. Hang, Z. Xing, X. Zhu, M. Yu, Y. Song, J. Zhu, Z. Liu, Dielectric properties and related ferroelectric domain configurations in multiferroic  $BiFeO_3$ - $BaTiO_3$  solid solutions, *Ceramics International*. 38 (2012) S411-S414.

[33] E. Antolini,  $\text{Li}_2\text{O}$  evaporation from  $\text{Li}_x\text{Co}_{1-x}\text{O}$  solid solutions at 1200 degrees C, *Ceramics International*. 27 (2001) 675-679.

[34] K. Zaara, M. Cheingui, V. Optasanu, M. Khitouni, Solid solution evolution during mechanical alloying in Cu-Nb-Al compounds, *International Journal of Minerals Metallurgy and Materials*. 26 (2019) 1129-1139.

[35] D. Li, Z. Yang, D. Jia, S. Wang, X. Duan, B. Liang, Q. Zhu, Y. Zhou, Structure evolution, amorphization and nucleation studies of carbon-lean to -rich SiBCN powder blends prepared by mechanical alloying, *RSC Advance* 6 (2016) 48255-48271.

## Figures

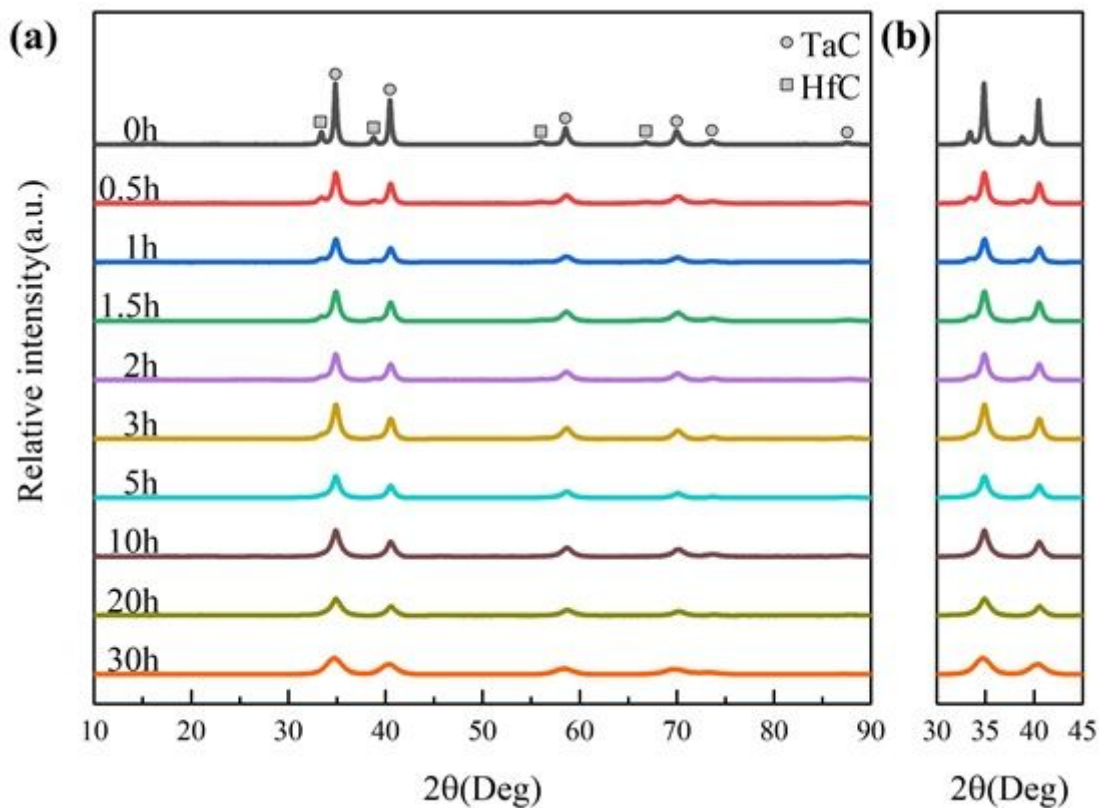


**Figure 1**

The XRD patterns of the TaC-HfC powder mixture after mechanical alloying for different time.

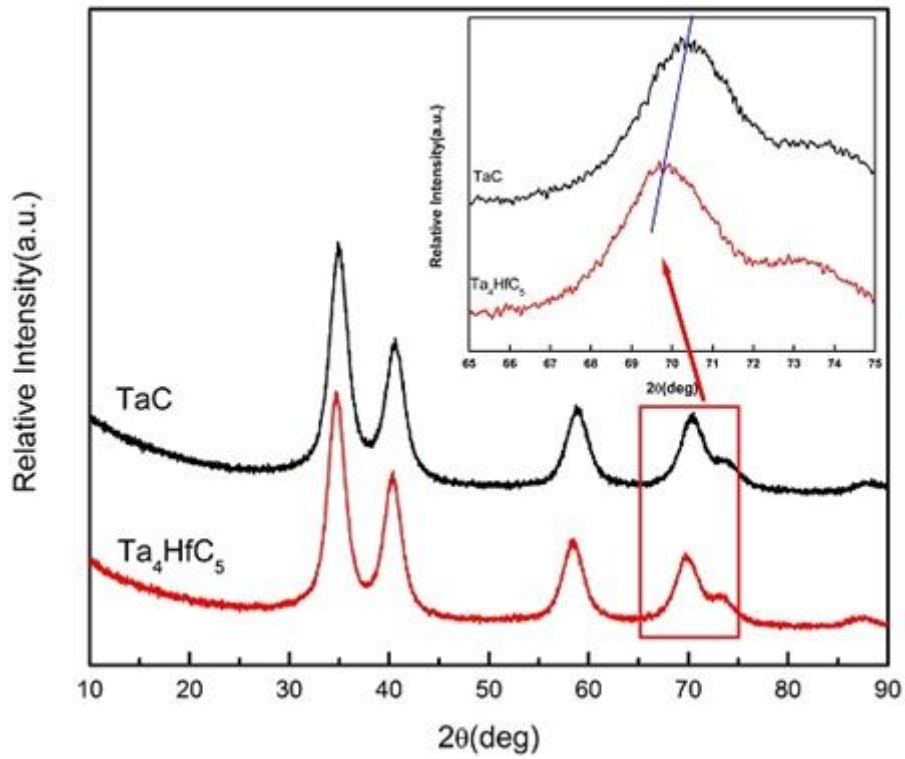


**Figure 2**

The XRD patterns of pure TaC powder and TaC-HfC powder mixture after mechanical alloying for 30 h, inserted is the magnifying picture.

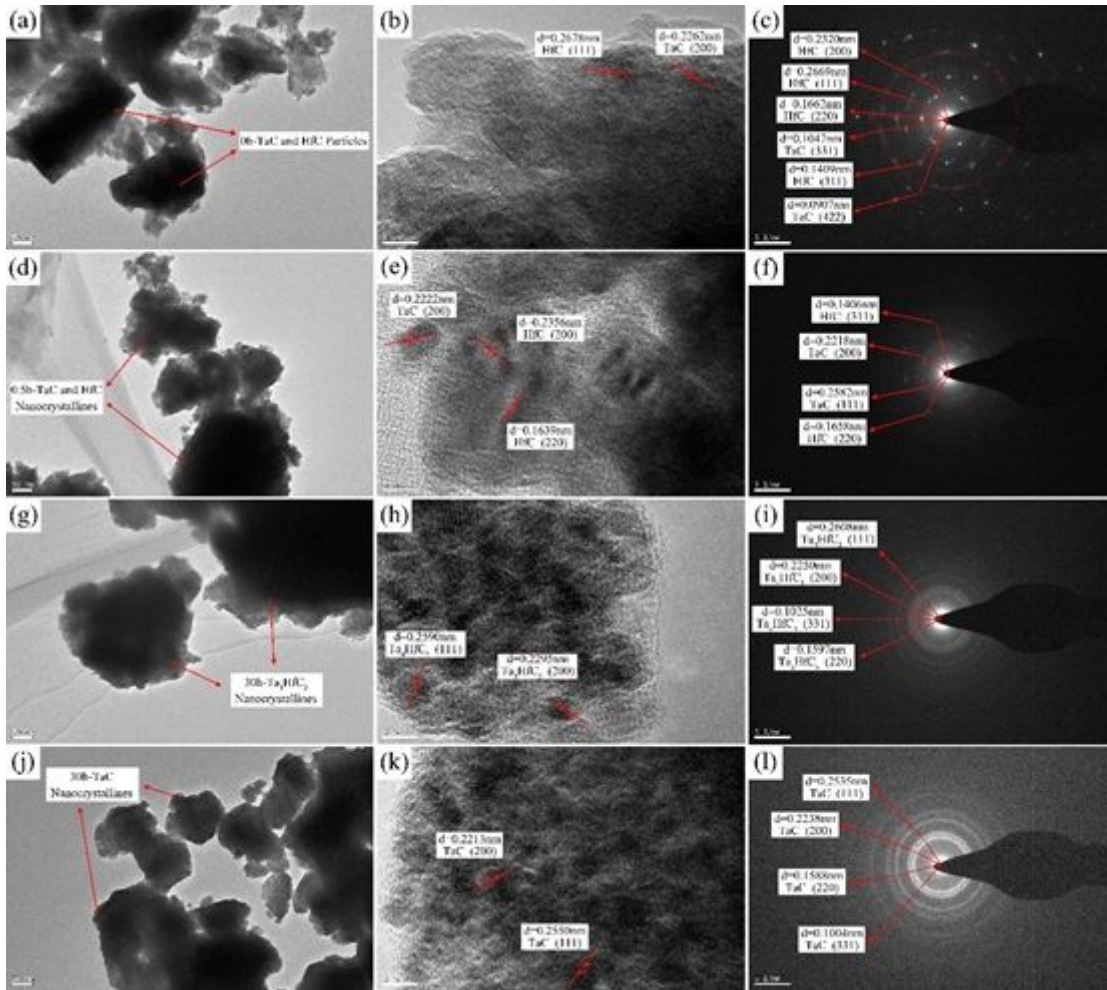


**Figure 3**

The TEM, HRTEM and electron diffraction pattern (SAED) images of the pure TaC powder and HfC-TaC powder mixture after mechanical alloying for different time. (a-c) HfC-TaC, 0 h; (d-f) HfC-TaC, 0.5 h; (g-i) HfC-TaC, 30 h; (j-l) pure TaC powder, 30 h.

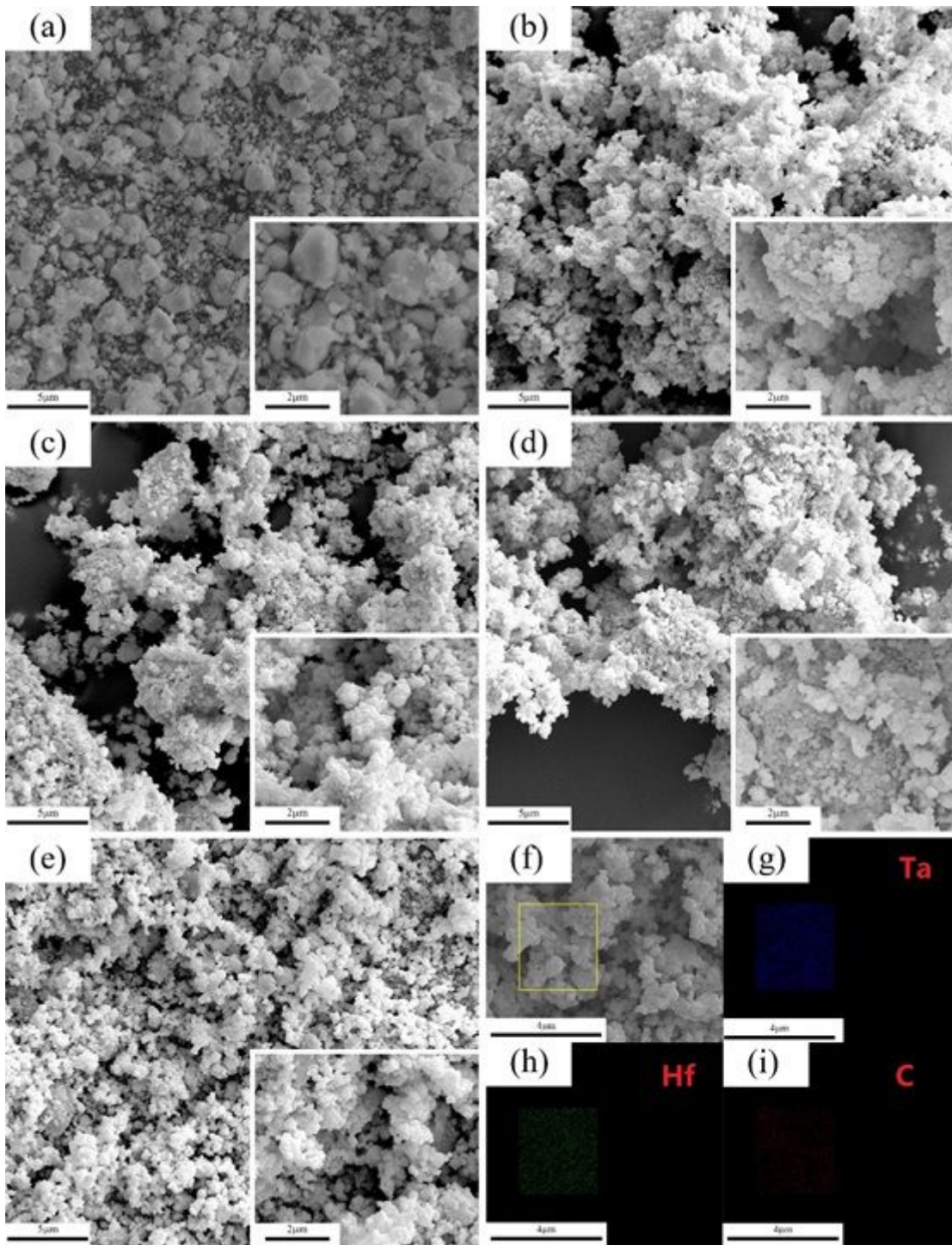


**Figure 4**

The SEM surface images of TaC-HfC mixed powders after mechanical alloying for different time. (a) 0 h; (b) 0.5 h; (c) 1.5 h; (d) 20 h; (e, f) 30 h; (g-i) the corresponding element maps, the inserted are the magnifying SEM images.

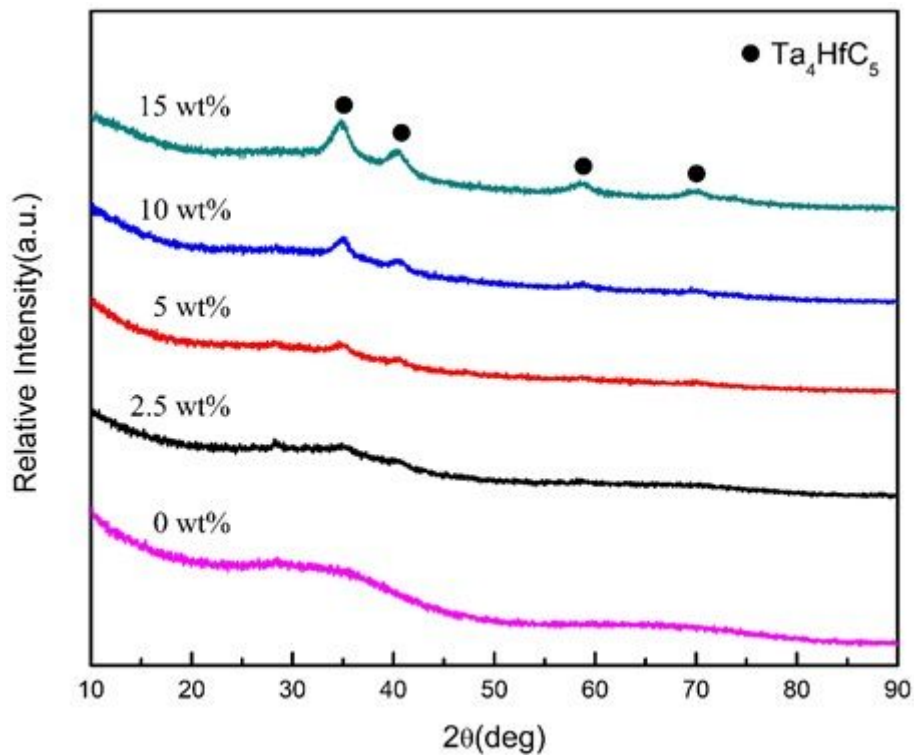


Figure 5

The XRD patterns of in situ SiBCN-Ta<sub>4</sub>HfC<sub>5</sub> amorphous-nanocrystalline composite powder with different Ta<sub>4</sub>HfC<sub>5</sub> content.

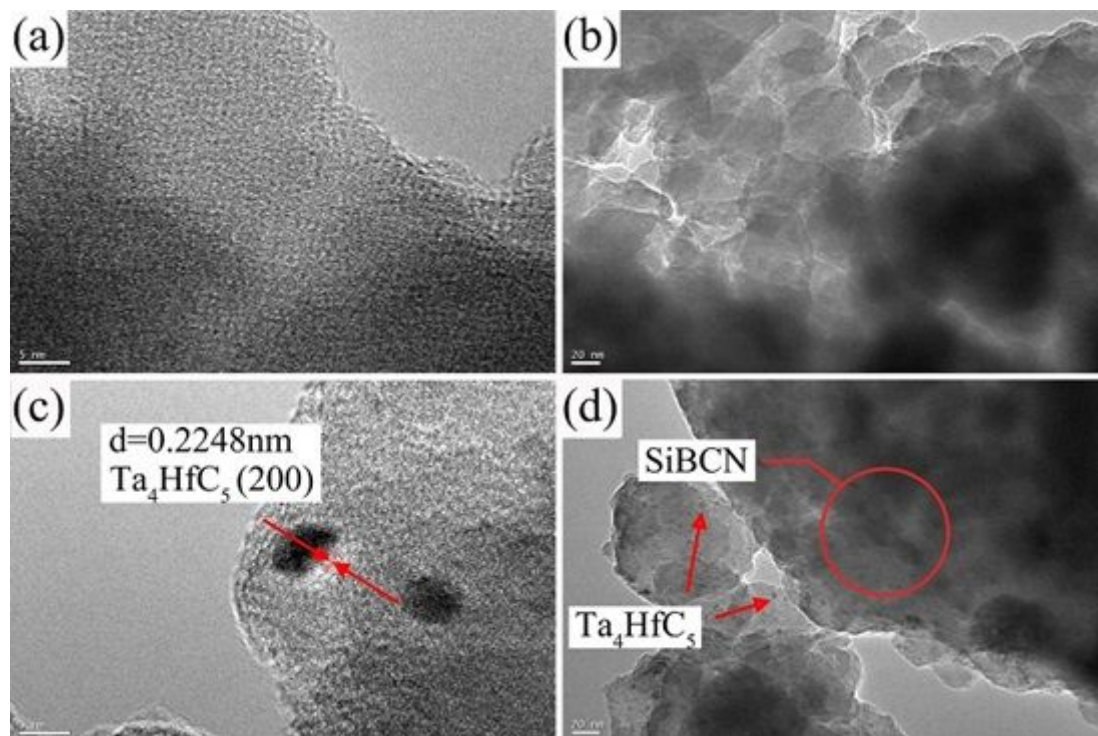


Figure 6

The TEM and HRTEM images of the (a-b) SiBCN amorphous powder and (c-d) SiBCN-Ta<sub>4</sub>HfC<sub>5</sub> amorphous-nanocrystalline composite powder.

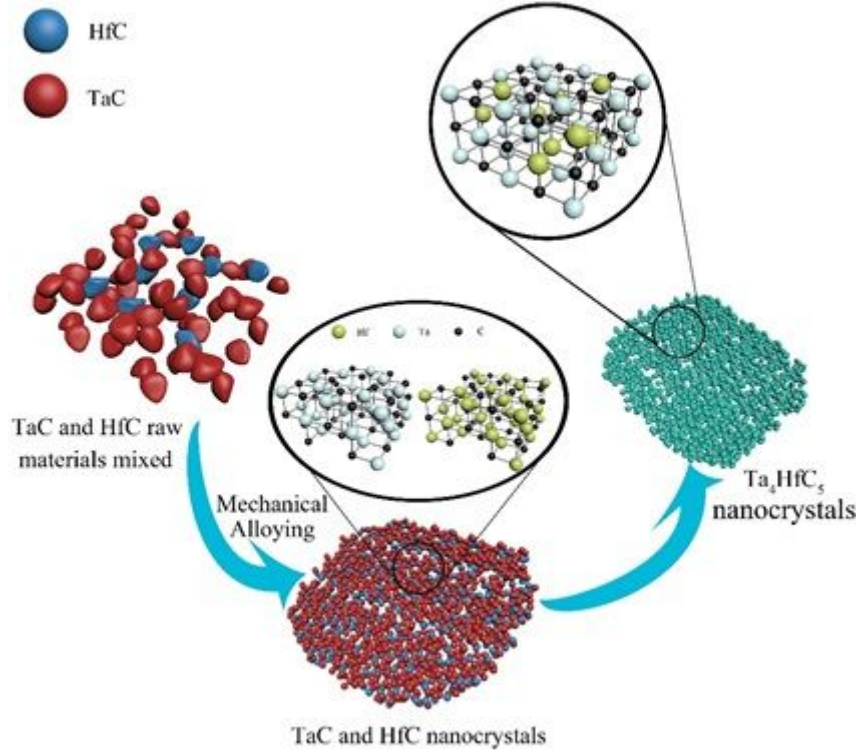


Figure 7

The formation mechanisms of the nano Ta<sub>4</sub>HfC<sub>5</sub> during mechanical alloying.

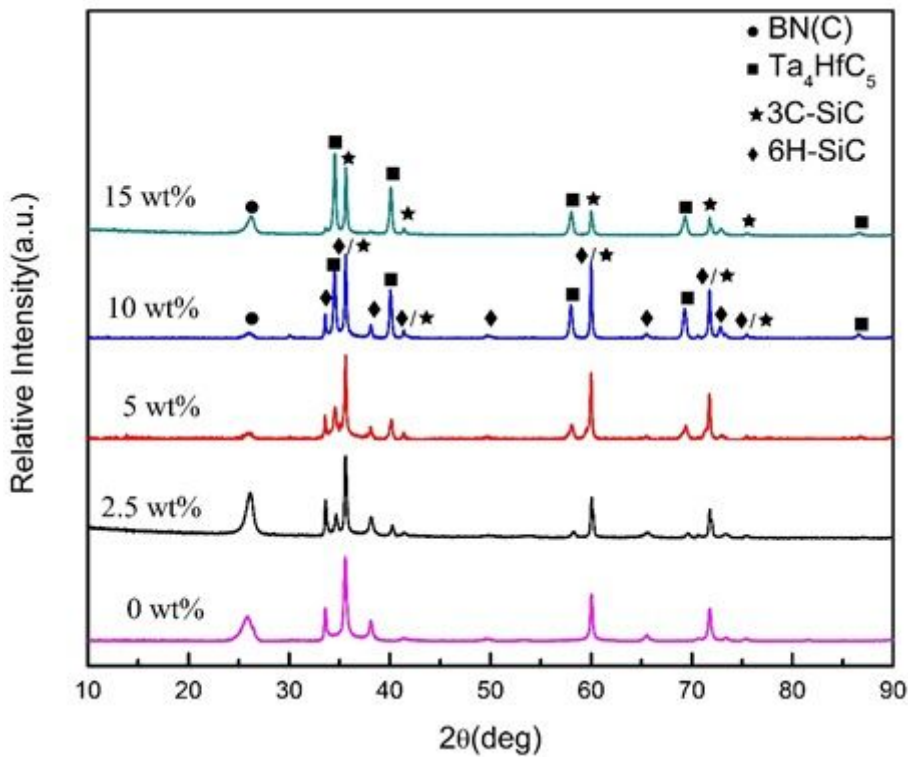
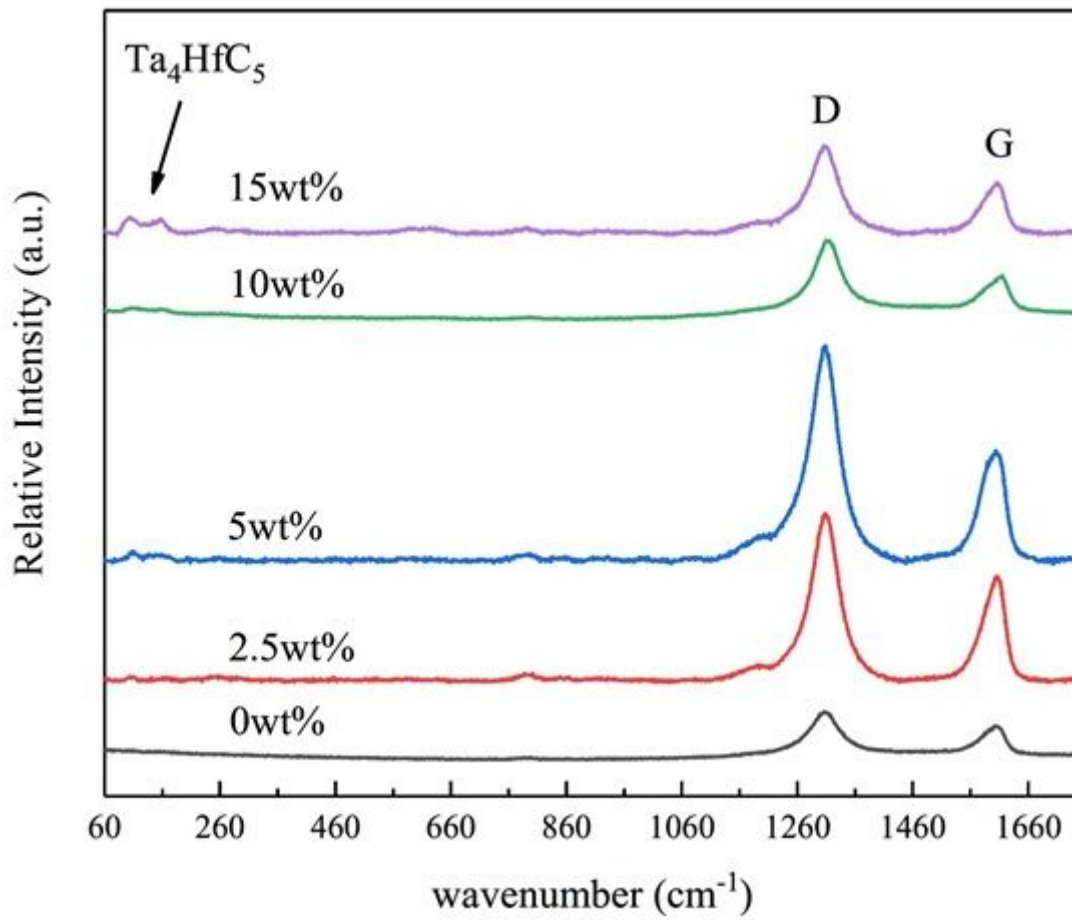


Figure 8

The XRD patterns of the as-sintered SiBCN-Ta<sub>4</sub>HfC<sub>5</sub> composite ceramics with different Ta<sub>4</sub>HfC<sub>5</sub> content.



**Figure 9**

The Raman spectra of the as-sintered SiBCN-Ta<sub>4</sub>HfC<sub>5</sub> composite ceramics with different Ta<sub>4</sub>HfC<sub>5</sub> content.

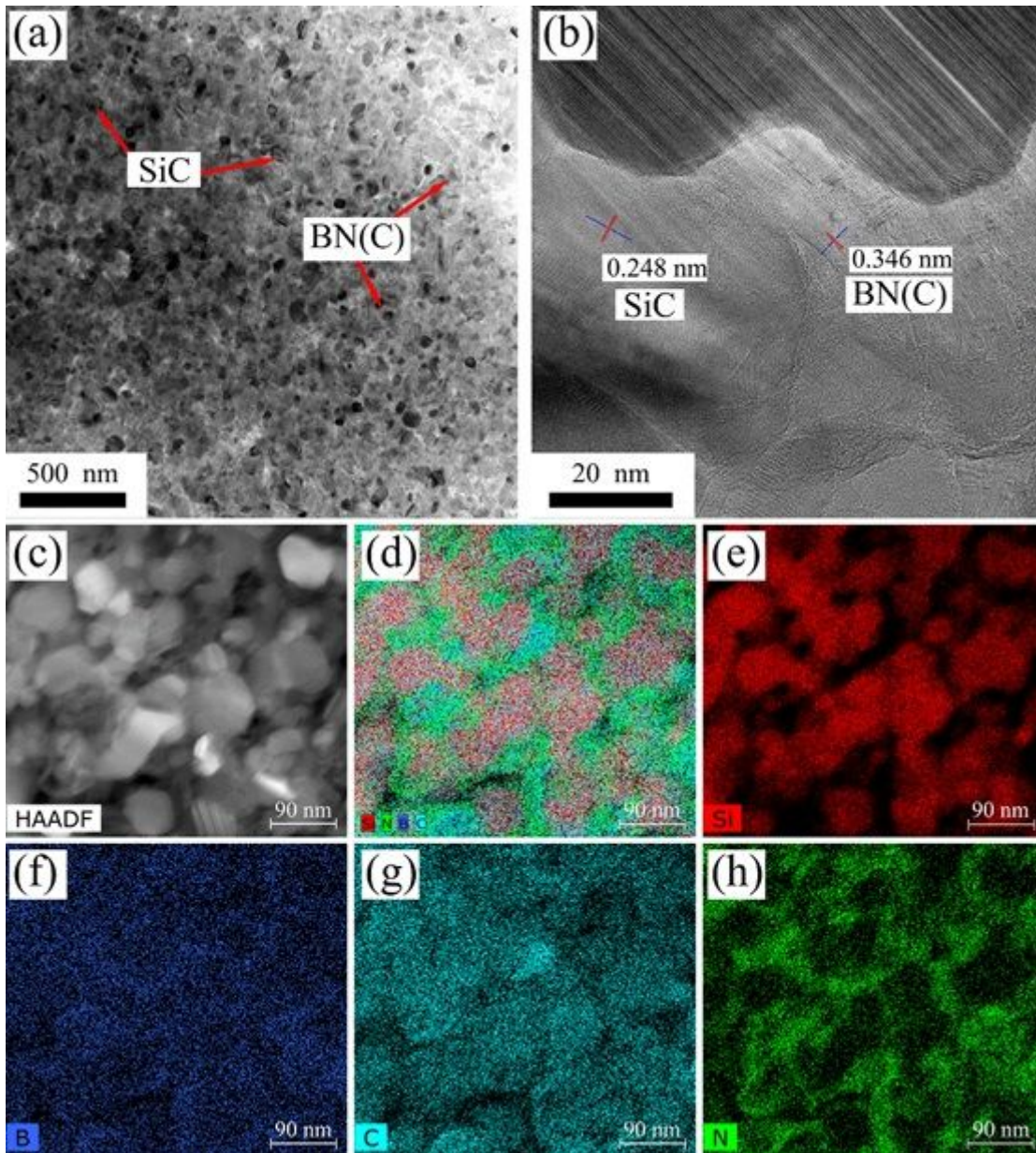


**Figure 10**

The TEM and HEM images of the pure SiBCN ceramics. (a-b) Bright-field images; (c)-(j) HAADF-STEM image and corresponding EDS maps.

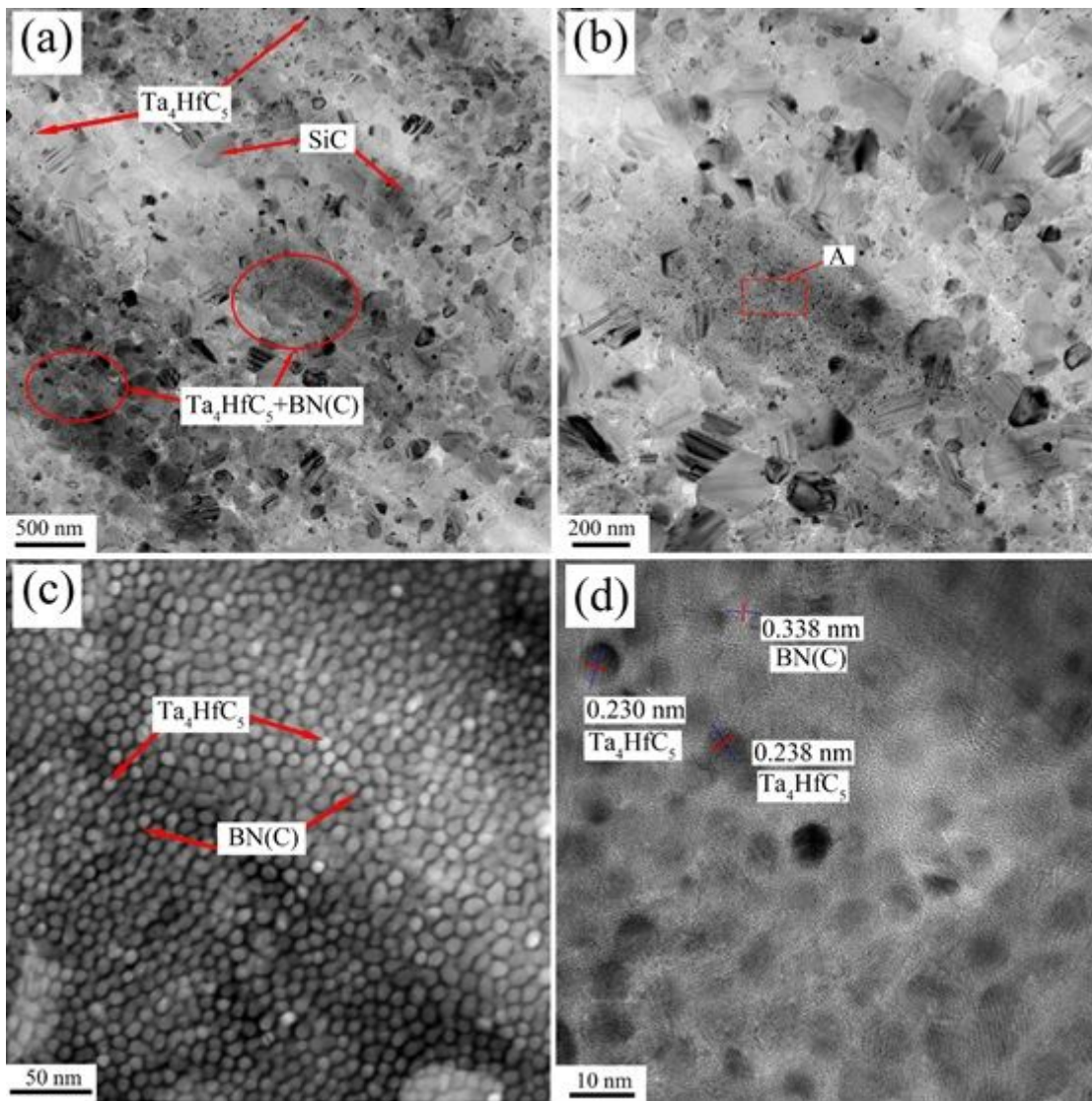


**Figure 11**

The TEM and HRTEM images of the SiBCN-Ta<sub>4</sub>HfC<sub>5</sub> composite ceramics with 2.5 wt% Ta<sub>4</sub>HfC<sub>5</sub>. (a-b) Bright-field images; (c) Magnifying TEM image of area A; (d) HRTEM image of area A.

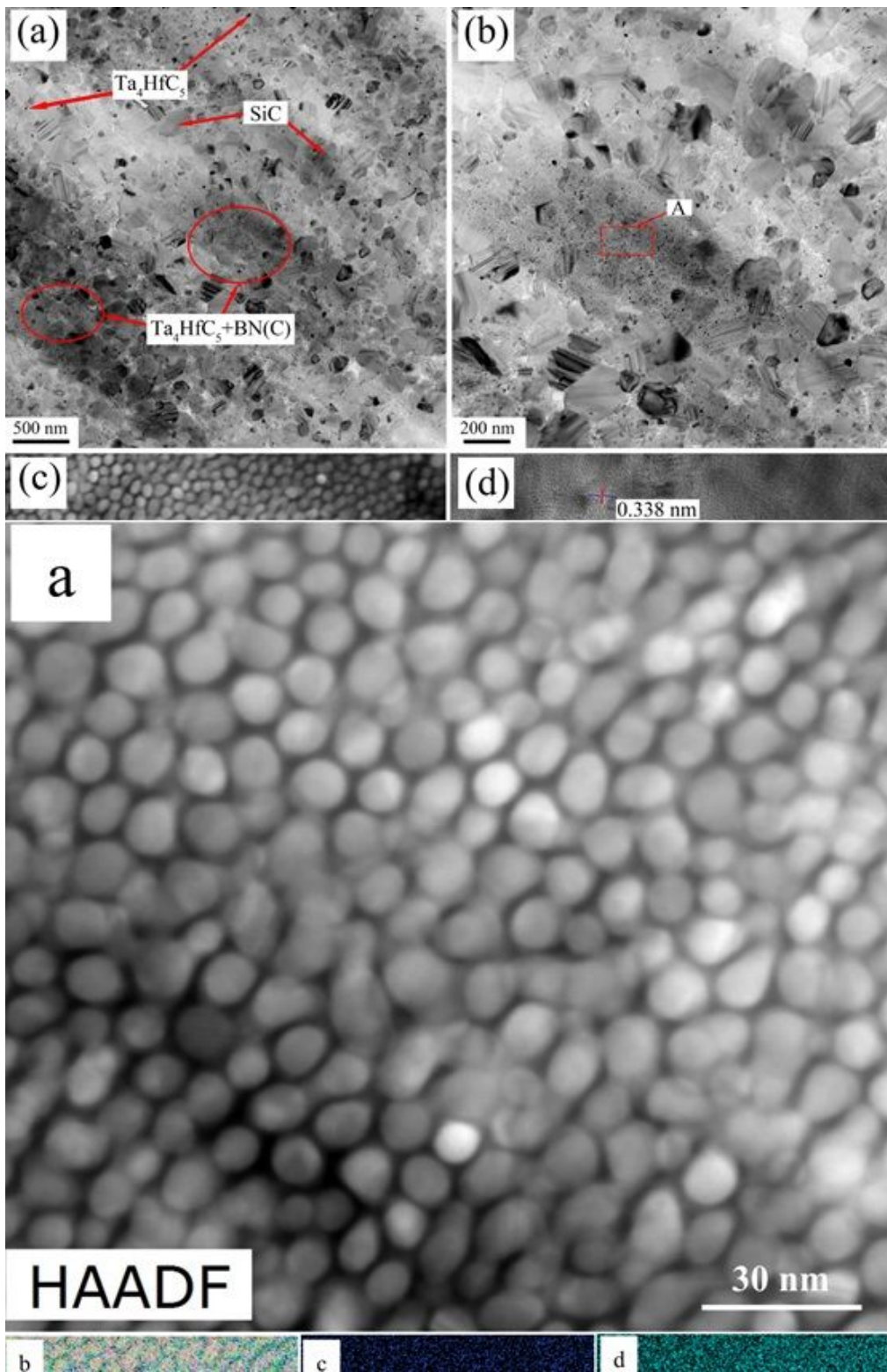
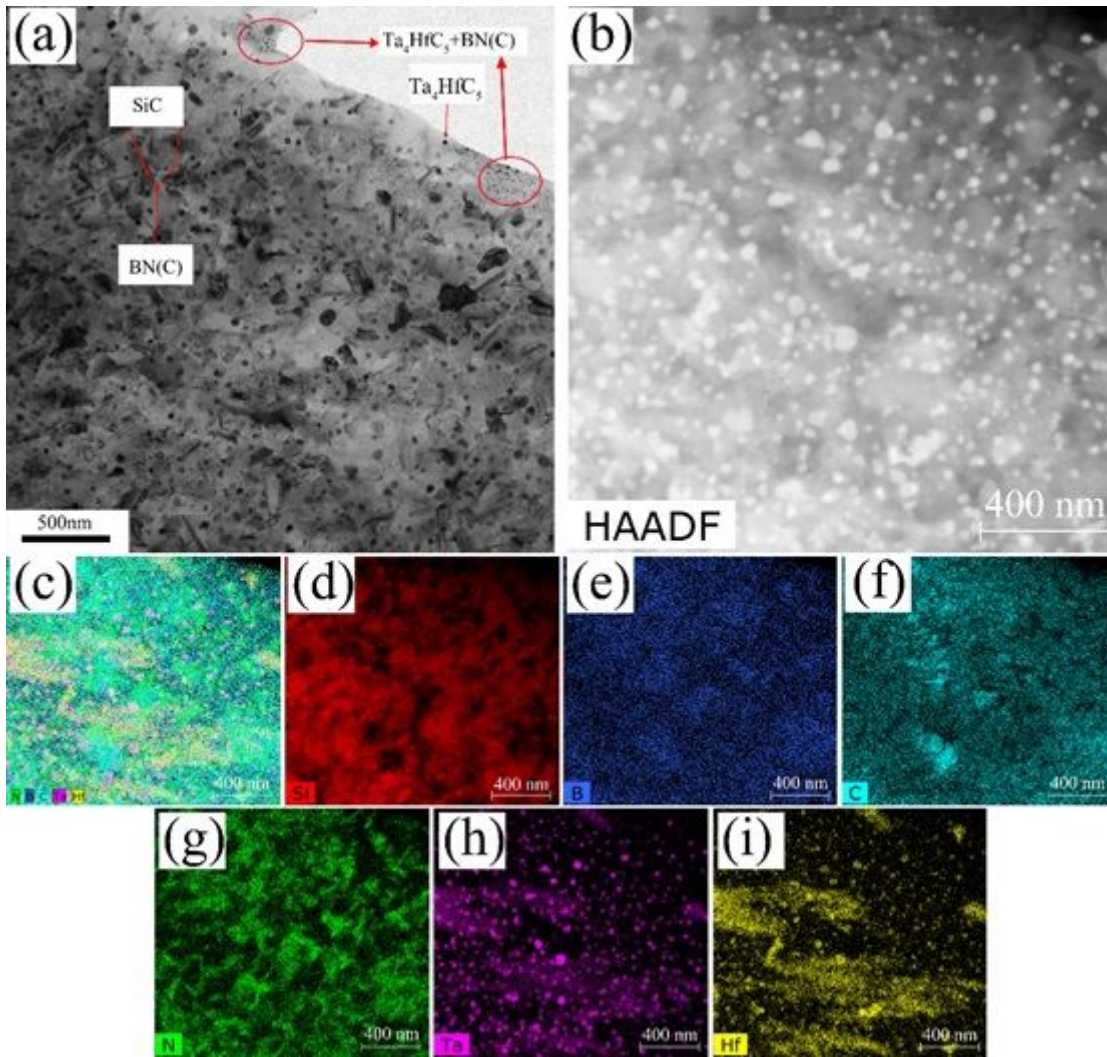


Figure 12

The selective EDS maps of Ta<sub>4</sub>HfC<sub>5</sub> distributed within BN(C) region for composite ceramics with 2.5 wt% Ta<sub>4</sub>HfC<sub>5</sub>.



**Figure 13**

The TEM images and EDS maps of the SiBCN-Ta<sub>4</sub>HfC<sub>5</sub> composite ceramics with 10 wt% Ta<sub>4</sub>HfC<sub>5</sub>. (a) Bright-field TEM image; (b) STEM image; (d)-(j) EDS maps.

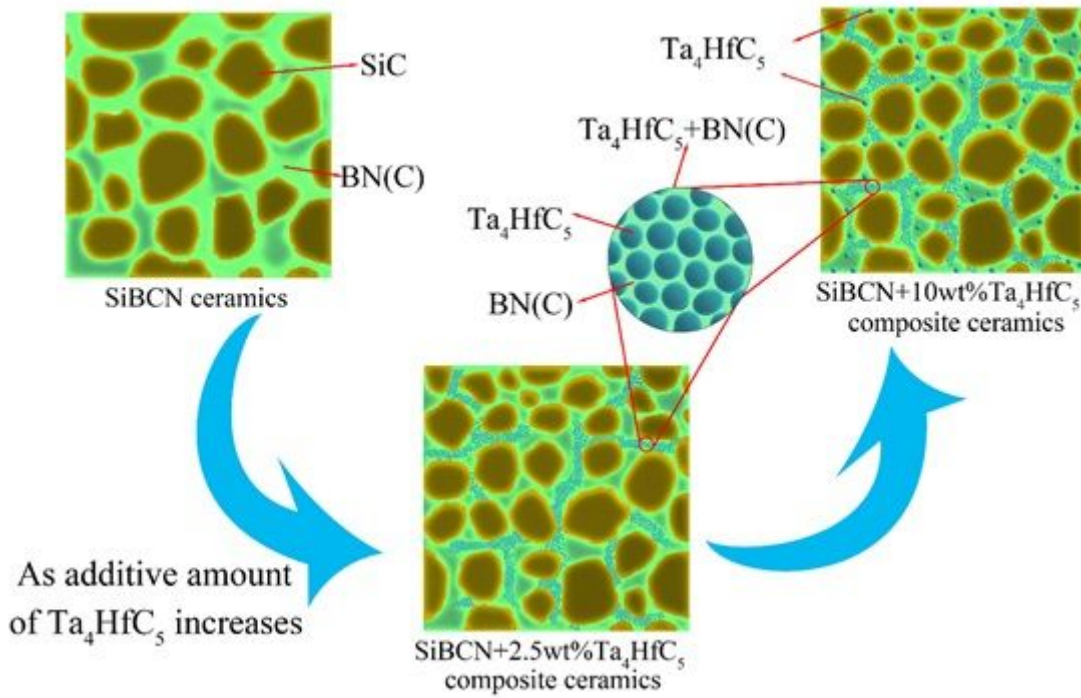


Figure 14

The schematic illustrating the microstructure evolution of Ta<sub>4</sub>HfC<sub>5</sub> distribution in composite ceramics with different Ta<sub>4</sub>HfC<sub>5</sub> addition

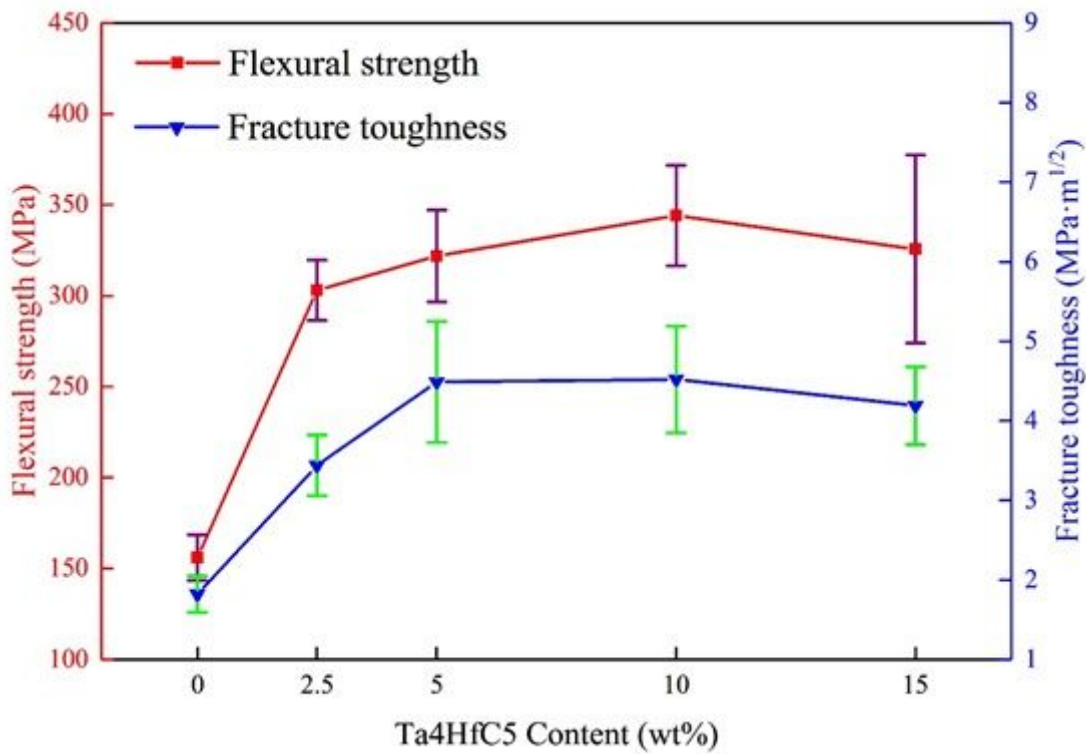


Figure 15

The flexural strength and fracture toughness of the as-sintered SiBCN-Ta<sub>4</sub>HfC<sub>5</sub> composite ceramics with different content of Ta<sub>4</sub>HfC<sub>5</sub>.

## Supplementary Files

This is a list of supplementary files associated with this preprint. Click to download.

- [Equations.pdf](#)